

Effects of Phosphorus and Carbon Contents on Amorphous Forming Ability in Fe-based Amorphous Alloys Used for Thermal Spray Coatings

JEONGHYEON DO, SEUNGMUN JUNG, HYUK-JOONG LEE, BYEONG-JOO LEE, GIL-UP CHA, CHANG YONG JO, and SUNGHAK LEE

Cost-effective Fe-based amorphous alloys used for thermal spray coatings were developed by varying contents of P and C, and their microstructure, hardness, and corrosion resistance were analyzed. In order to achieve chemical compositions having high amorphous forming ability, thermodynamically calculated phase diagrams of Fe-Al-P-C-B five-component system were used, from which compositions of super-cooled liquid having the lowest driving force of formation of crystalline phases were obtained. The thermodynamic calculation results showed that only phases of Fe_3P and Fe_3C were formed in the $\text{Fe}_{78}\text{Al}_2\text{P}_{(18.3-x)}\text{C}_x\text{B}_{1.7}$ alloy system. Considering driving force curves of Fe_3P and Fe_3C , the carbon contents were selected to be 6.90 and 7.47 at. pct, when the thermodynamic calculation temperatures were 697 K (414 °C) and 715 K (442 °C), respectively. According to the microstructural analysis of suction-cast alloys, the $\text{Fe}_{78}\text{Al}_2\text{P}_{10.83}\text{C}_{7.47}\text{B}_{1.7}$ alloy showed a fully amorphous microstructure, whereas the $\text{Fe}_{78}\text{Al}_2\text{P}_{11.40}\text{C}_{6.9}\text{B}_{1.7}$ and $\text{Fe}_{78}\text{Al}_2\text{P}_{10.3}\text{C}_{8.0}\text{B}_{1.7}$ alloys contained Fe_3P and Fe_3C phases. This $\text{Fe}_{78}\text{Al}_2\text{P}_{10.83}\text{C}_{7.47}\text{B}_{1.7}$ alloy showed the better hardness and corrosion resistance than those of conventional thermal spray coating alloys, and its production cost could be lowered using cheaper alloying elements, thereby leading to the practical application to amorphous thermal spray coatings.

DOI: 10.1007/s11661-013-1615-0

© The Minerals, Metals & Materials Society and ASM International 2013

I. INTRODUCTION

AMORPHOUS alloys have excellent characteristics such as strength, stiffness, magnetism, and corrosion resistance because atoms are aligned like in a liquid. Since amorphous alloys with high amorphous forming abilities were first developed by conventional casting methods in the 1990s, a number of alloys such as La-Ni-Al,^[1] Zr-Al-Cu-Ni,^[2,3] Zr-Ti-Cu-Ni-Be,^[4,5] Zr-Ti-Cu-Ni,^[6] and Cu-Ti-Zr-Ni-Sn-Si^[7] alloys have been developed with renewed attention. In particular, Zr-Ti-Cu-Ni-Be^[8] alloys show excellent amorphous forming ability (critical cooling rate; about 1 K/s), hardness, strength, stiffness, and corrosion resistance,^[5,9] and thus have been used as components of electrical products or sporting goods. However, the manufacturing cost is still high because of the requirement of a vacuum environ-

ment during casting, and the size and shape of the products are limited.^[10,11] In addition, amorphous alloys have poor ductility and toughness because the brittle fracture readily occurs due to formation of highly localized shear bands.^[12] Thus, if the fabrication method of amorphous/metal coatings, in which the surface consists of an amorphous alloy and the interior substrate consists of a ductile metal having sufficient ductility and fracture toughness, can be developed, this brittle problem can be solved, while fully taking advantages of amorphous alloys.

Thermal spraying methods including high velocity oxyfuel (HVOF) use a mixture of oxygen and fuel which is combusted and accelerated through a nozzle. The HVOF process is widely applied in industries because (1) they have very high spray rate and deposition efficiency, (2) they consume fuel gases which are inexpensive and easily obtainable, (3) they require minimum preheating and cooling during spraying, and (4) they are readily applicable to production lines.^[13,14] Ferrous amorphous coatings fabricated by the HVOF process have improved the resistance to wear and corrosion^[15,16] because of formation of amorphous phases when completely molten ferrous amorphous powders are contacted with a substrate at very fast cooling rates of about 10^7 K/s.^[17] They are cost effective in simultaneously reducing the wear and corrosion on the surface of various parts such as boiler, pumps, impellers, and pulleys in power generation industries.^[18]

Asami *et al.*^[19] confirmed the applicability of ferrous amorphous coatings by investigating the corrosion

JEONGHYEON DO, formerly Research Assistant with Center for Advanced Aerospace Materials, Pohang University of Science and Technology, Pohang 790-784, Korea, is now Senior Researcher with Advanced Metallic Materials Division, Korea Institute of Materials Science, Changwon 642-831, Korea. SEUNGMUN JUNG and HYUK-JOONG LEE, Research Assistants, BYEONG-JOO LEE and SUNGHAK LEE, Professors, are with Center for Advanced Aerospace Materials, Pohang University of Science and Technology. Contact e-mail: shlee@postech.ac.kr GIL-UP CHA, Team Leader, is with Rolling Facilities Group, Pohang Works, POSCO Pohang 790-785 Korea. CHANG YONG JO, Director, is with Advanced Metallic Materials Division, Korea Institute of Materials Science.

Manuscript submitted July 16, 2012.

Article published online February 1, 2013

resistance of Fe-Cr-, Fe-Co-, and Fe-Ni-based amorphous alloys. Kishitake *et al.*^[20] fabricated ferrous amorphous coatings by low-pressure plasma spraying of Fe-Cr-based amorphous alloys. These ferrous amorphous alloys were somewhat expensive because they contained a considerable amount of expensive alloying elements of Co, Ni, or Cr. In addition, they did not have sufficient amorphous forming ability, and thus the complete formation of amorphous phases might not be achieved during the coating process. Therefore, the development of ferrous amorphous alloys which contain cost-effective alloying elements and have sufficient amorphous forming ability is essentially needed for applications of their thermal spray coatings of various industrial areas.

The objective of the present research was to develop new cost-effective Fe-based amorphous alloys in order to apply these alloys to the thermal spray coatings. To achieve chemical compositions of these alloys having high amorphous forming ability, thermodynamically calculated phase diagrams of Fe-Al-P-C-B five-component system^[21,22] were used, from which compositions of super-cooled liquid having the lowest driving force of formation of crystalline phases such as Fe₃C, α -Fe, γ -Fe, Fe₃P, and Fe₂₃C₆ could be obtained. Several representative alloys having the highest amorphous forming ability (having the lowest driving force of formation of crystalline phases) were fabricated using a suction casting technique, and their microstructure, hardness, and corrosion resistance were analyzed.

II. EXPERIMENTAL

A. Alloy Design of Fe-based Amorphous Alloys

One of the major parameters determining amorphous forming ability in Fe-based amorphous alloys is a ratio of metallic elements and metalloid elements. It can be learned from the previous research^[23] that Fe-based amorphous alloys are basically made by bonding between metallic and metalloid elements in an atomic level. Thus, thermodynamic calculations are conducted in this study to estimate the amorphous forming ability when the ratio of metallic element of Fe and metalloid elements was 80:20. P, C, and B are selected as constituent metalloid elements. C and P proved to be inevitably added elements for amorphous forming in Fe-based amorphous alloys.^[24] In particular, P plays a role in preventing the formation of brittle meta-stable phases such as Fe₂₃B₆ and in enhancing the amorphous forming ability without adding expensive alloying elements.^[25] The content of B is set to be relatively low at 1.7 at. pct in consideration of the high price of an Fe-B ferroalloy. In addition, 2.0 at. pct of Al is added for improving amorphous forming ability because Al expands the supercooled liquid region (ΔT_x).^[26] Accordingly, the representative alloy composition is determined to be Fe₇₈Al₂P_{(18.3-x)}}C_xB_{1.7}}. Here, the variables are P and C because an appropriate combination of P and C can effectively enhance the amorphous forming ability. Since Fe₃C and Fe₃P generally have a high driving force for

formation in Fe-P-C-based alloys,^[27] their formation behavior should be carefully monitored by thermodynamic calculations.

B. Fabrication of Fe-based Amorphous Alloys

Fe-based alloys designed by thermodynamic calculations were fabricated by a suction casting method. Master alloys were produced by arc melting of appropriate amounts of pure metals of Fe (99.9 pct), Al (99.99 pct), and C (99 pct) (RND Korea Co., Korea) and ferroalloys of Fe-B (99.2 pct) and Fe-P (98.5 pct) (CIQ, China) in a water-cooled copper crucible under a Ti-gettered argon atmosphere. Each master alloy of about 25 g in weight was melted three or four times to insure the compositional homogeneity. Rods having 1.2 mm in diameter and 50 mm in length (weight; about 0.4 g) were produced in a water-cooled copper mold by suction casting under an argon atmosphere.

C. Microstructural Analysis and Hardness Test

The cast alloys were polished in diamond pastes (size: 0.25 μ m), etched by a Viella's solution (45 ml Glycerol, 15 ml HNO₃, and 30 ml HCl), and observed by a scanning electron microscope (SEM, model: JSM-6330F, Jeol, Japan). Phases present in the alloys were analyzed by X-ray diffraction (XRD, Cu radiation, scan rate; 2 deg min⁻¹, scan step size; 0.02 deg, angle range; 30 deg $\leq 2\theta \leq$ 100 deg) and wavelength dispersive spectroscopy (WDS, acceleration voltage; 15 kV, beam current; 5 $\times 10^{-8}$ Amp, interval; 0.06 \times 0.06). Overall bulk hardness was measured by a Vickers hardness tester under a 100 g load.

D. Corrosion Test (Potentiodynamic Polarization Test)

A corrosion cell was used for open circuit potential (OCP) measurements and potentiodynamic polarization tests in an aerated 1 pct NaCl solution at room temperature. A saturated calomel electrode (SCE) was used as a reference electrode and two parallel high-density graphite rods were served as counter electrodes for the current measurement. Cast specimens (rod diameter; 1.2 mm) were mounted by a non-conductive macromolecule resin so that they could be connected to electrodes. The schematic diagram of the modified potentiodynamic polarization test is shown in Figure 1. The OCP was measured after a delay of 30 min for the specimens to reach a steady state. Then, the specimen was potentiodynamically polarized at a scan rate of 0.0004 V/s from -0.25 V below the OCP to +1.2 V above the SCE potential.

III. RESULTS AND DISCUSSION

A. Interpretation of Amorphous Forming Ability by Thermodynamic Calculation

To seek alloy compositions with high amorphous forming ability, a thermodynamic calculation scheme,^[28]

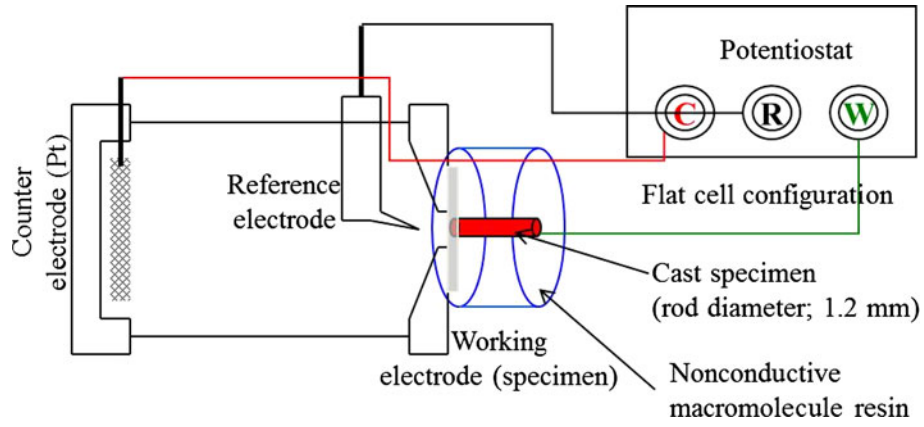


Fig. 1—Schematic diagram showing the modified potentiodynamic polarization test.

Table I. Thermodynamic Parameters for Fe₃(P,B) Compound Phase

Formula Unit: Fe ₃ (P,B) ₁	Ref.
${}^{\circ}G_{\text{Fe:P}}^{\text{e}} = -186514 + 472.847T - 85.61T \ln T$	[32]
${}^{\circ}G_{\text{Fe:B}}^{\text{e}} = {}^{\circ}G_{\text{Fe:B}}^{\text{cementite}} + 85000$	This work
$L_{\text{Fe:P,B}}^{\text{e}} = -130000$	This work
${}^{\circ}G_{\text{Fe:B}}^{\text{cementite}} = -80233.85 + 12.24544$ $+ 3\text{GHSEFE} + \text{GHSEBB}$	[31]

where a composition of super-cooled liquid with the lowest driving force of formation for other crystalline phases is selected, was used. For the present Fe-Al-P-C-B five-component system, the Gibbs energy of the liquid alloy, for example, can be expressed as follows:

$$\begin{aligned}
 G_{\text{m}} = & x_{\text{Fe}} {}^{\circ}G_{\text{Fe}} + x_{\text{Al}} {}^{\circ}G_{\text{Al}} + x_{\text{P}} {}^{\circ}G_{\text{P}} + x_{\text{C}} {}^{\circ}G_{\text{C}} + x_{\text{B}} {}^{\circ}G_{\text{B}} \\
 & + RT(x_{\text{Fe}} \ln x_{\text{Fe}} + x_{\text{Al}} \ln x_{\text{Al}} + x_{\text{P}} \ln x_{\text{P}} \\
 & + x_{\text{C}} \ln x_{\text{C}} + x_{\text{B}} \ln x_{\text{B}}) + x_{\text{Fe}x_{\text{Al}}} L_{\text{Fe,Al}} \\
 & + x_{\text{Fe}x_{\text{P}}} L_{\text{Fe,P}} + x_{\text{Fe}x_{\text{C}}} L_{\text{Fe,C}} + x_{\text{Fe}x_{\text{B}}} L_{\text{Fe,B}} \\
 & + x_{\text{Al}x_{\text{P}}} L_{\text{Al,P}} + x_{\text{Al}x_{\text{C}}} L_{\text{Al,C}} + x_{\text{Al}x_{\text{B}}} L_{\text{Al,B}} \\
 & + x_{\text{P}x_{\text{C}}} L_{\text{P,C}} + x_{\text{P}x_{\text{B}}} L_{\text{P,B}} + x_{\text{C}x_{\text{B}}} L_{\text{C,B}} \\
 & + x_{\text{Fe}x_{\text{Al}x_{\text{P}}} L_{\text{Fe,Al,P}} + x_{\text{Fe}x_{\text{Al}x_{\text{C}}} L_{\text{Fe,Al,C}} \\
 & + x_{\text{Fe}x_{\text{Al}x_{\text{B}}} L_{\text{Fe,Al,B}} + x_{\text{Fe}x_{\text{P}x_{\text{C}}} L_{\text{Fe,P,C}} \\
 & + x_{\text{Fe}x_{\text{P}x_{\text{B}}} L_{\text{Fe,P,B}} + x_{\text{Fe}x_{\text{C}x_{\text{B}}} L_{\text{Fe,C,B}} \\
 & + x_{\text{Al}x_{\text{P}x_{\text{C}}} L_{\text{Al,P,C}} + x_{\text{Al}x_{\text{P}x_{\text{B}}} L_{\text{Al,P,B}} \\
 & + x_{\text{Al}x_{\text{C}x_{\text{B}}} L_{\text{Al,C,B}} + x_{\text{P}x_{\text{C}x_{\text{B}}} L_{\text{P,C,B}}.
 \end{aligned} \quad [1]$$

Here, ${}^{\circ}G_i$ and x_i represent the Gibbs free energy of pure liquid i and mole fraction of i , respectively, and $L_{i,j}$ represents excess energy between elements i and j . The fourth or higher order interactions are not considered in Eq. [1]. Thermodynamic calculations were carried out using the ThermoCalc software^[29] and the upgraded version of thermodynamic database, TCFE2000.^[30,31] In the current database, Fe₃P is modeled as a stoichiometric compound,^[32] while experimental information^[33]

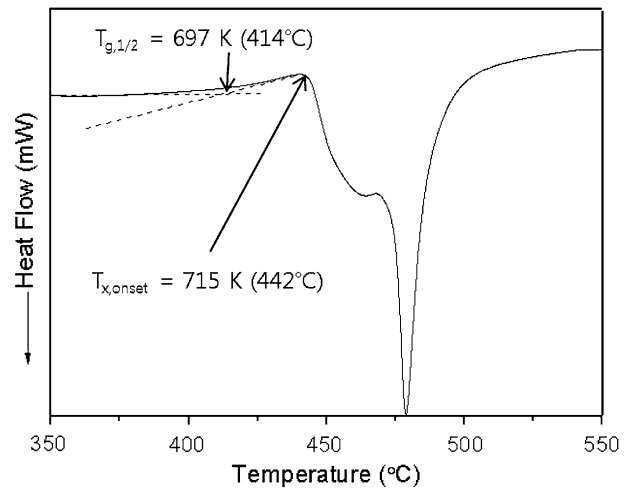


Fig. 2—Differential scanning calorimetry (DSC) thermogram of the alloy having mean composition (Fe₇₈Al₂P_{9.3}C₉B_{1.7}) of the representative alloy (Fe₇₈Al₂P_(18.3-x)C_xB_{1.7}) at a heating rate of 10 K/min. The glass transition temperature (T_g) and crystallization temperature ($T_{x,\text{onset}}$) are 697 K (414 °C) and 715 K (442 °C), respectively.

shows a non-negligible solubility of B replacing the P site. Therefore, in the present work, the thermodynamic model for the Fe₃P phase was extended into Fe₃(P,B) so that the solubility of B can be represented. The newly defined thermodynamic parameters for Fe₃(P,B) were adjusted (see Table I) so that the experimentally observed solubility of B in equilibrium with Fe₂B, which is stoichiometric,^[33] is correctly reproduced.

In order to determine the temperature, which is one of the important parameters calculating driving force of phase formation, a differential scanning calorimetry (DSC) analysis was conducted on an alloy having mean composition (Fe₇₈Al₂P_{9.3}C₉B_{1.7}) of the representative alloy (Fe₇₈Al₂P_(18.3-x)C_xB_{1.7}). Figure 2 shows a thermogram of the alloy at a heating rate of 10 K/min. From this thermogram, the glass transition temperature (T_g) and crystallization temperature ($T_{x,\text{onset}}$) were measured to be 697 K (414 °C) and 715 K (442 °C), respectively.

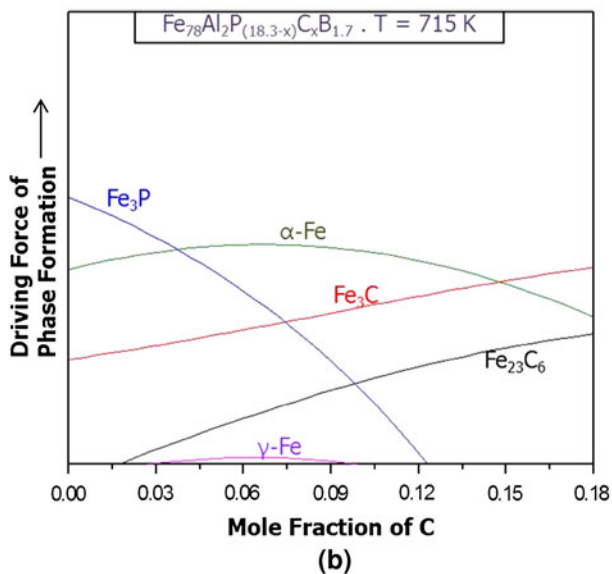
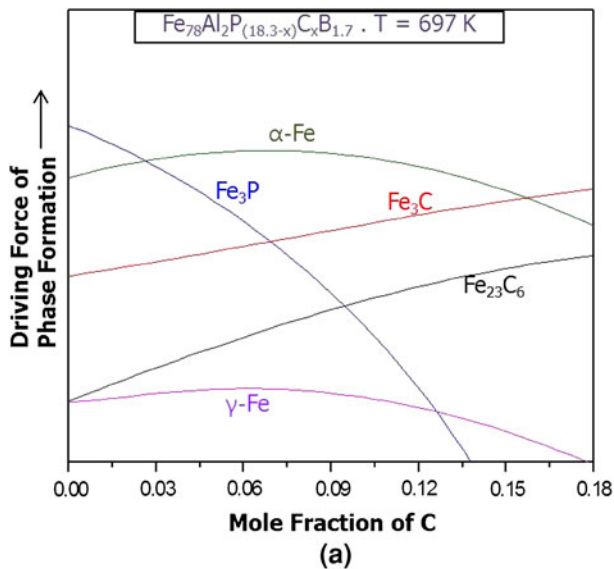


Fig. 3—Driving force curves of formation of Fe_3C , $\alpha\text{-Fe}$, $\gamma\text{-Fe}$, Fe_3P , and Fe_{23}C_6 in the $\text{Fe}_{78}\text{Al}_2\text{P}_{(18.3-x)}\text{C}_x\text{B}_{1.7}$ alloy system at (a) 697 K and (b) 715 K as a function of mole fraction of C. These curves were calculated by an analysis program of ThermoCalc on the basis of the upgraded version of TCFE2000.

Figures 3(a) and (b) show driving force curves of formation of Fe_3C , $\alpha\text{-Fe}$, $\gamma\text{-Fe}$, Fe_3P , and Fe_{23}C_6 in the $\text{Fe}_{78}\text{Al}_2\text{P}_{(18.3-x)}\text{C}_x\text{B}_{1.7}$ alloy system at 697 K (414 °C) and 715 K (442 °C), respectively, as a function of mole fraction of C. The driving forces of formation of Fe_3C , Fe_3P , Fe_{23}C_6 , and $\alpha\text{-Fe}$ are relatively high at 697 K (414 °C) and 715 K (442 °C), while that of $\gamma\text{-Fe}$ is low. This indicates that the possibility of formation of Fe_3C , Fe_3P , Fe_{23}C_6 , and $\alpha\text{-Fe}$ phases is high in the $\text{Fe}_{78}\text{Al}_2\text{P}_{(18.3-x)}\text{C}_x\text{B}_{1.7}$ alloy system. Since these driving force data might not be matched with the experimental data of actual phase formation, the preliminary experiments of casting and phase analysis are essentially needed.

Four Fe-based alloys, the carbon contents of which were varied at 6, 9, 12, and 15 at. pct, were made in a rod

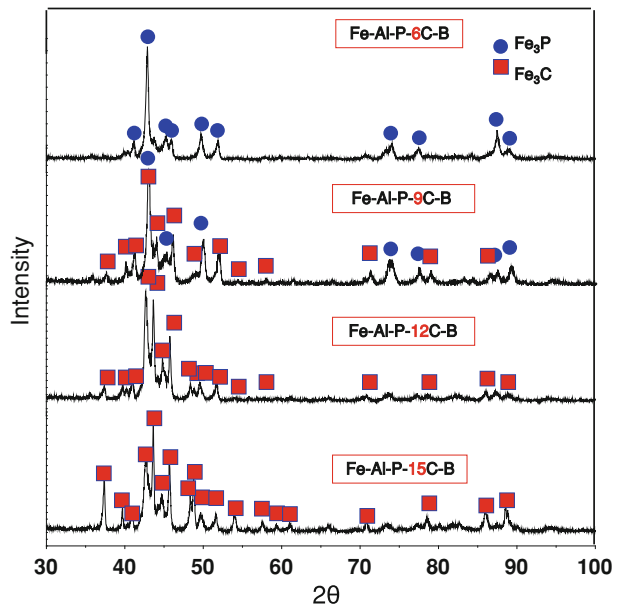


Fig. 4—X-ray diffraction (XRD) patterns of the four Fe-based alloys, the carbon contents of which were varied at 6, 9, 12, and 15 at. pct in the representative alloy ($\text{Fe}_{78}\text{Al}_2\text{P}_{(18.3-x)}\text{C}_x\text{B}_{1.7}$), showing peaks of Fe_3P and Fe_3C .

shape (diameter; 4 mm, length; 50 mm) by suction casting. Figure 4 shows the X-ray diffraction (XRD) analysis data of the four alloys. Peaks of Fe_3P are observed in the Fe-Al-P-6C-B alloy, but disappear as the carbon content increases. When the carbon content exceeds 12 at. pct, peaks of Fe_3C are found without peaks of Fe_3P . These XRD data indicate that only phases of Fe_3P and Fe_3C are formed without $\alpha\text{-Fe}$, $\gamma\text{-Fe}$, and Fe_{23}C_6 phases in the $\text{Fe}_{78}\text{Al}_2\text{P}_{(18.3-x)}\text{C}_x\text{B}_{1.7}$ alloy system. This is because the actual driving forces for formation of $\alpha\text{-Fe}$, $\gamma\text{-Fe}$, and Fe_{23}C_6 phases might be quite reduced below the calculated driving forces by some reasons or factors which were not considered in the thermodynamic calculation. Thus, driving force curves of formation of $\alpha\text{-Fe}$, $\gamma\text{-Fe}$, and Fe_{23}C_6 are eliminated from Figs. 3(a) and (b), as shown in Figures 5(a) and (b). Considering both driving force curves of Fe_3P and Fe_3C , the intersection of the two curves indicates the composition at which driving forces of Fe_3P and Fe_3C are minimized, while the possibility of forming amorphous phases is maximized, as marked by arrows in Figures 5(a) and (b). From the compositions located at curve intersections, the carbon contents are selected to be 6.90 and 7.47 at. pct when the thermodynamic calculation temperatures are 697 K (414 °C) and 715 K (442 °C), respectively. According to this thermodynamic calculation, the final alloy compositions, at which the amorphous forming ability is maximized, are determined to be $\text{Fe}_{78}\text{Al}_2\text{P}_{11.40}\text{C}_{6.9}\text{B}_{1.7}$ and $\text{Fe}_{78}\text{Al}_2\text{P}_{10.83}\text{C}_{7.47}\text{B}_{1.7}$.

B. Microstructure of Fe-based Alloys

Four Fe-based alloys having aforementioned compositions ($\text{Fe}_{78}\text{Al}_2\text{P}_{11.40}\text{C}_{6.9}\text{B}_{1.7}$ and $\text{Fe}_{78}\text{Al}_2\text{P}_{10.83}\text{C}_{7.47}\text{B}_{1.7}$), together with the other two compositions of

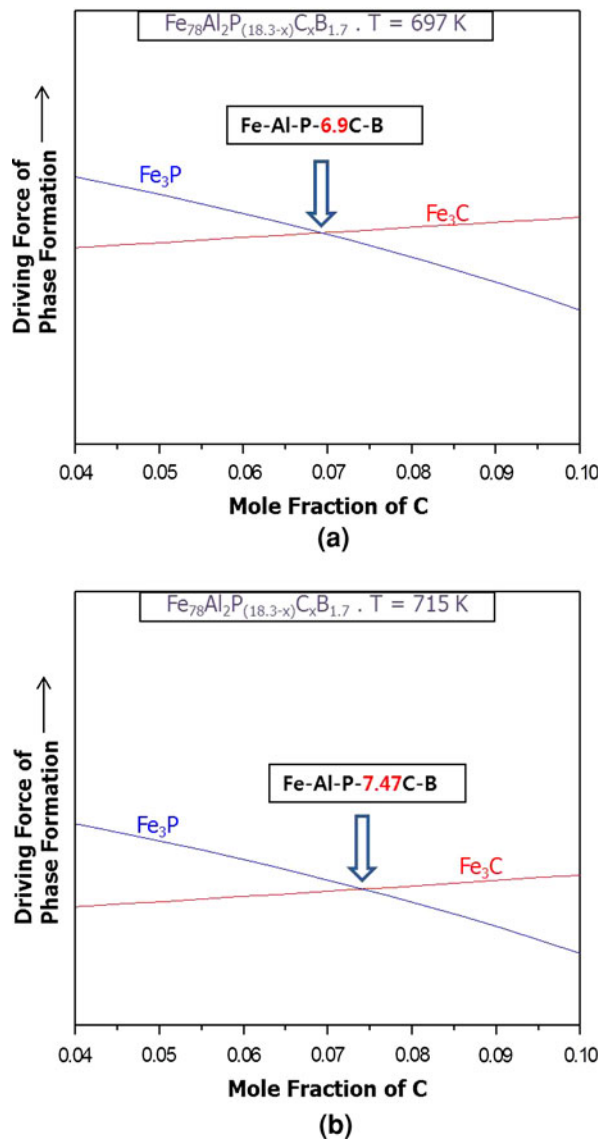


Fig. 5—Driving force curves of formation of Fe_3P and Fe_3C in the $\text{Fe}_{78}\text{Al}_2\text{P}_{(18.3-x)}\text{C}_x\text{B}_{1.7}$ alloy system at (a) 697 K and (b) 715 K as a function of mole fraction of C. Driving force curves of formation of α -Fe, γ -Fe, and Fe_3P are eliminated from Figs. 3(a) and (b). From the compositions located at curve intersections, as indicated by arrows, the carbon contents are selected to be 6.90 and 7.47 at. pct when the thermodynamic calculation temperatures are 697 K (414 °C) and 715 K (442 °C), respectively.

$\text{Fe}_{78}\text{Al}_2\text{P}_{10.3}\text{C}_{8.0}\text{B}_{1.7}$ and $\text{Fe}_{78}\text{Al}_2\text{P}_{11.3}\text{C}_{9.0}\text{B}_{1.7}$, were made in a rod shape (diameter; 1.2 mm, length; 50 mm) by suction casting. For convenience, Fe-based alloys having compositions of $\text{Fe}_{78}\text{Al}_2\text{P}_{11.40}\text{C}_{6.9}\text{B}_{1.7}$, $\text{Fe}_{78}\text{Al}_2\text{P}_{10.83}\text{C}_{7.47}\text{B}_{1.7}$, $\text{Fe}_{78}\text{Al}_2\text{P}_{10.3}\text{C}_{8.0}\text{B}_{1.7}$, and $\text{Fe}_{78}\text{Al}_2\text{P}_{11.3}\text{C}_{9.0}\text{B}_{1.7}$ are referred to as 6.9C, 7.47C, 8.0C, and 9.0C alloys, respectively, according to the C content. Figure 6 shows the XRD analysis data of the four alloys. These data are somewhat different from the XRD data of Figure 4 because the cooling rate of 1.2-mm-diameter suction-cast rods is faster than that of the 4-mm-diameter suction-cast rods. Peaks of Fe_3P as well as hollow patterns of amorphous phase are found in the

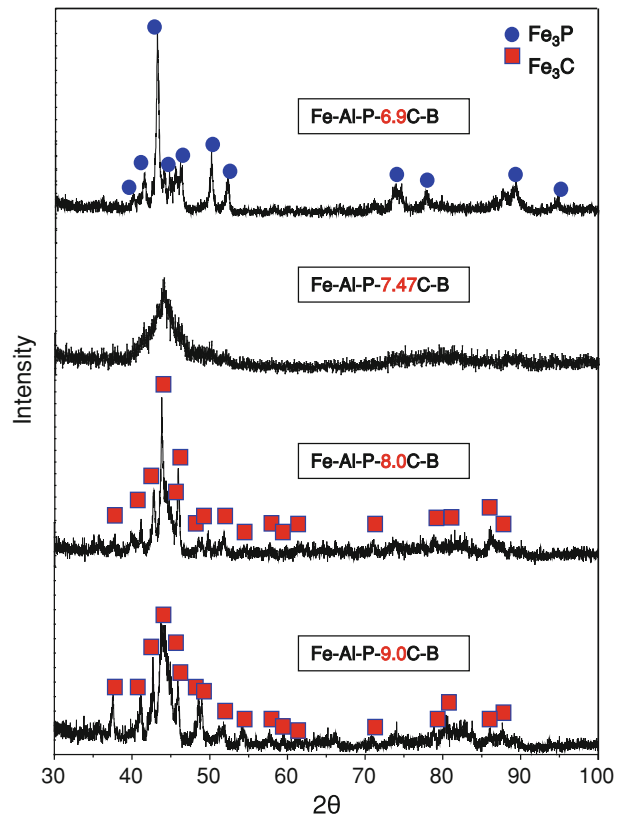


Fig. 6—X-ray diffraction (XRD) patterns of the 6.9C ($\text{Fe}_{78}\text{Al}_2\text{P}_{11.40}\text{C}_{6.9}\text{B}_{1.7}$), 7.47C ($\text{Fe}_{78}\text{Al}_2\text{P}_{10.83}\text{C}_{7.47}\text{B}_{1.7}$), 8.0C ($\text{Fe}_{78}\text{Al}_2\text{P}_{10.3}\text{C}_{8.0}\text{B}_{1.7}$), and 9.0C ($\text{Fe}_{78}\text{Al}_2\text{P}_{11.3}\text{C}_{9.0}\text{B}_{1.7}$) alloys, showing peaks of Fe_3P and Fe_3C as well as broad hollow patterns.

6.9C alloy, but only broad patterns are observed in the 7.47 alloy without peaks of Fe_3P . In the 8.0C and 9.0C alloys containing the higher content of C, peaks of Fe_3C appear, together with hollow patterns.

Figures 7(a) through (c) are SEM microstructures of the 6.9C, 7.47C, and 8.0C alloys. In the 6.9C and 8.0C alloys, crystalline phases are found in a dendritic shape, and their size is relatively large at a few micrometers in size (Figures 7(a) and (c)), whereas they are not observable in the 7.47C alloy (Figure 7(b)). The WDS analysis results of the 6.9C and 8.0C alloys are shown in Table II and are compared with the overall compositions of 6.9 and 8.0 alloys measured from the wet chemical analysis method. In the 6.9C alloy, the P content is higher in crystalline phases than in the amorphous matrix, while the C contents are not much varied. This implies that crystalline phases in the 6.9C alloy are P-containing compounds, which can be identified to be Fe_3P , and are well matched with the XRD data of Figure 6. Crystalline phases in the 8.0C alloy are identified to be Fe_3C because they contain the higher content of C than the amorphous matrix. These WDS analysis data are well matched with the XRD data.

It is noted that the microstructure of the 7.47C alloy is matched with the thermodynamically calculated data at 715 K of Figure 5(b), whereas that of 6.9C alloy is not matched with the data at 697 K of Figure 5(a) because the 6.9C alloy contains crystalline phases. The reason

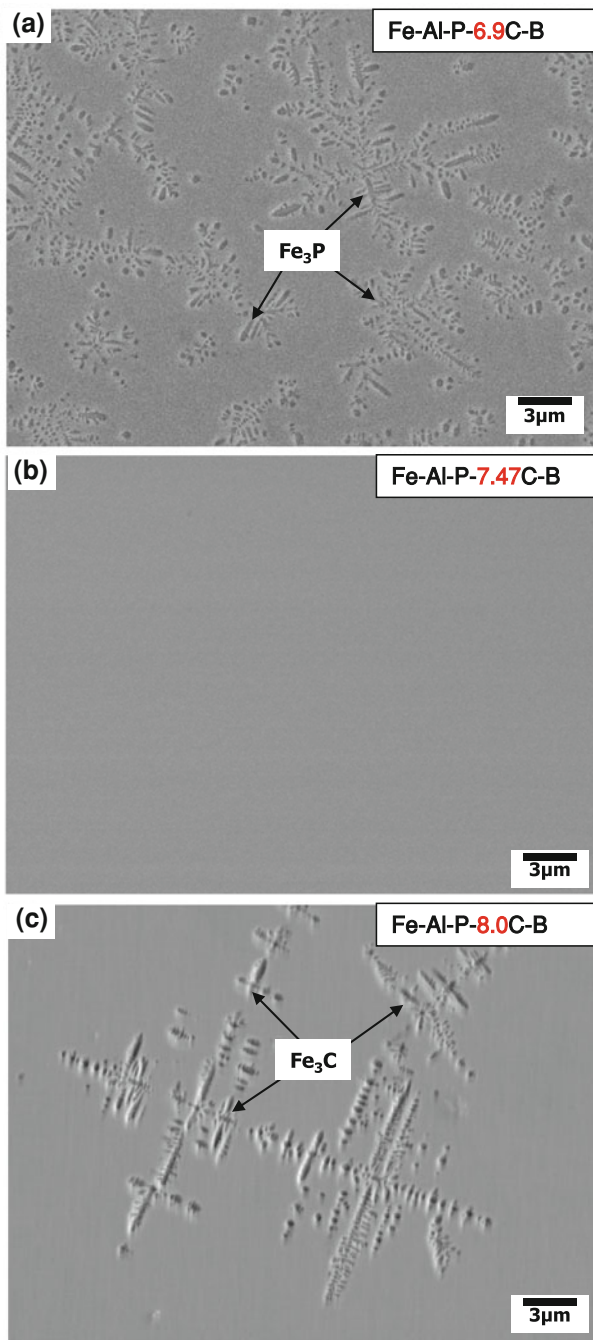


Fig. 7—SEM micrographs of the (a) 6.9C ($\text{Fe}_{78}\text{Al}_2\text{P}_{11.40}\text{C}_{6.9}\text{B}_{1.7}$), (b) 7.47C ($\text{Fe}_{78}\text{Al}_2\text{P}_{10.83}\text{C}_{7.47}\text{B}_{1.7}$), and (c) 8.0C ($\text{Fe}_{78}\text{Al}_2\text{P}_{10.3}\text{C}_{8.0}\text{B}_{1.7}$) alloys, showing crystalline phases of Fe_3P and Fe_3C distributed in the amorphous matrix of the 6.9C and 8.0C alloys, respectively.

for the unmatched microstructure with the thermodynamically calculated data is associated with the importance of calculation temperature in the estimation of amorphous forming ability. It means that the driving force of formation calculated at the crystallization temperature (715 K) is meaningful for the estimation of amorphous forming ability. When the liquid phase of the 6.9C alloy is rapidly cooled, a small amount of the crystalline phase is formed in a dendritic shape prior to

the formation of amorphous matrix. Thus, the driving force calculated at the glass transition temperature (697 K), at which the glass transition actively occurs, is not useful for estimating amorphous forming ability, but the driving force calculated at the crystallization temperature, at which the formation of amorphous phase starts, representatively determines the amorphous forming ability of the present alloys.

In order to find the difference between the calculated and actual crystallization temperatures, the DSC analysis was conducted on the 7.47C alloy at a heating rate of 10 K/min, and a thermogram of the alloy is shown in Figure 8. The glass transition temperature (T_g) and crystallization temperature ($T_{x,\text{onset}}$) are 699 K (417 °C) and 716 K (443 °C), respectively. When these temperatures are compared with those of the $\text{Fe}_{78}\text{Al}_2\text{P}_{9.3}\text{C}_9\text{B}_{1.7}$ alloy (Figure 2), the crystallization temperature of the 7.47C alloy is almost the same as that of the $\text{Fe}_{78}\text{Al}_2\text{P}_{9.3}\text{C}_9\text{B}_{1.7}$ alloy, although there is a difference in glass transition temperatures (3 deg). Thus, the temperature of 715 K is reasonably accepted as an accurate temperature for thermodynamic calculation of amorphous forming ability in this alloy system.

C. Hardness and Corrosion Resistance of Fe-based Alloys

The Vickers hardness values of the 6.9C, 7.47C, 8.0C, and 9.0C alloys are 1048(± 38), 1061(± 20), 1054(± 50), and 1052(± 17) VHN, respectively. These hardness values show better hardness than those of conventional thermal spray coating alloys.^[20,34] The 7.47C alloy composed of amorphous phase shows a slightly higher hardness than the other alloys containing crystalline phases. The hardness of the four alloys is higher than 1000 VHN, and the hardness difference between alloys is not large. This is because crystalline phases of Fe_3P and Fe_3C are quite hard and their volume fractions are low.

A potentiodynamic polarization curve of the 7.47C alloy is shown in Figure 9 and is compared with that of the Fe-Cr-based alloy^[20] (composition; Fe-10Cr-13P-7C (at. pct)) and a hastelloy C22 alloy (composition; Ni-22Cr-13Mo-3.0Fe-3.0W-2.5Co-0.5Mn-0.35V-0.08Si-0.01C (wt pct)) which are commercially used as thermal spray coating alloys.^[35] Table III lists corrosion potential (E_o) and corrosion current density (i_o) obtained from the polarization curves. These results are unable to represent the absolute values because the modified potentiodynamic polarization test is not the standard corrosion test. However, this test facilitates the relative comparison of corrosion resistance. The corrosion current density does not rapidly increase in the 7.47 alloy with increasing corrosion potential because it is an amorphous alloy in which grain boundaries do not exist.^[36-40] The corrosion current density was measured from intersection points of two Tafel lines of polarization curves. Since i_o of the alloys is very low, the corroded amount arising from the simple immersion is hardly observed. i_o of the 7.47C alloy is lower than that of the Fe-Cr-P-C alloy and the hastelloy C22. E_o is higher in the 7.47C alloy than in the Fe-Cr-P-C alloy and hastelloy C22. It can be concluded from the data of

Table II. WDS Analysis Results of the 6.9C (Fe₇₈Al₂P_{11.40}C_{6.9}B_{1.7}) and 8.0C (Fe₇₈Al₂P_{10.3}C_{8.0}B_{1.7}) Alloys (Unit: at. pct)

Alloy	Detected Area	Fe	P	C
6.9C	matrix	80.49	10.67	6.14
	crystalline phase	75.54	14.18	7.59
	alloy composition*	78.24	11.29	6.82
8.0C	matrix	79.14	10.70	7.47
	crystalline phase	76.77	9.62	10.91
	alloy composition*	78.21	10.22	7.91

* Overall alloy composition measured by wet chemical analysis.

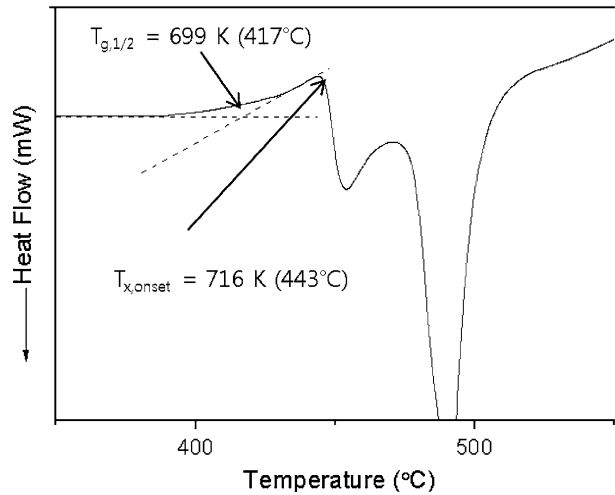


Fig. 8—Differential scanning calorimetry (DSC) thermogram of the 7.47C (Fe₇₈Al₂P_{10.83}C_{7.47}B_{1.7}) alloy at a heating rate of 10 K/min. The glass transition temperature (T_g) and crystallization temperature ($T_{x,onset}$) are 699 K (417 °C) and 716 K (443 °C), respectively.

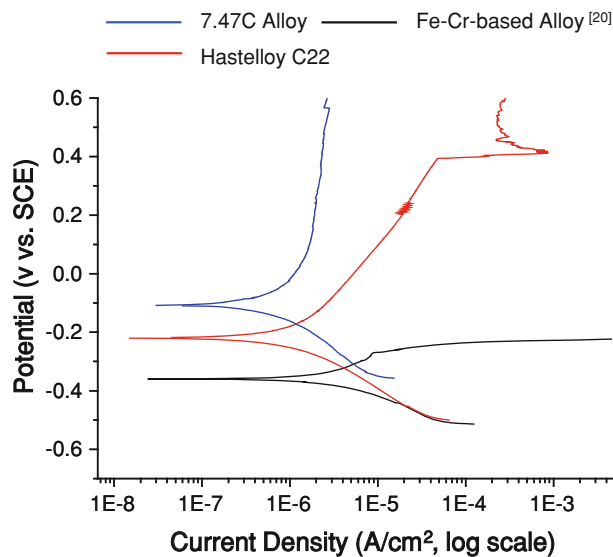


Fig. 9—Potentiodynamic polarization curves of the 7.47C (Fe₇₈Al₂P_{10.83}C_{7.47}B_{1.7}) alloy, Fe-Cr-based alloy,^[20] and hastelloy 22 alloys. The alloy specimens were immersed in a 1 pct NaCl solution at room temperature.

Table III. Potentiodynamic Polarization Test Results of the 7.47C (Fe₇₈Al₂P_{10.83}C_{7.47}B_{1.7}) Alloy, Fe-Cr-Based Alloy (Composition; Fe-10Cr-13P-7C (at. pct)),^[20] and Hastelloy C22

Alloy	E_0 (V _{SCE})	i_0 (μA/cm ²)	Relative Price Percentage (pct)
7.47C Alloy	-0.108	0.156	100
Fe-Cr-P-C Alloy	-0.366	2.497	118
Hastelloy C22	-0.220	0.720	1527

i_0 and E_0 that the corrosion resistance of the 7.47C alloy is better than that of the Fe-Cr-P-C alloy and the hastelloy C22.

Table II shows the relative price percentage of alloying elements in comparison to the price of the 7.47C alloy. These standard prices were estimated by prices of ferroalloys on the basis of the LME (London Metal Exchange) daily price (at the date of January 13th of 2012).^[4] The price of alloying elements contained in the 7.47C alloys is lower than that contained in the commercial Fe-Cr-P-C alloy. It is also much lower than that contained in the hastelloy C22. This implies that the Fe-Cr-P-C alloy or hastelloy 22 can be sufficiently replaced by the present alloys. Simultaneously considering hardness and corrosion resistance and economic feasibilities required for amorphous thermal spray coatings, the present alloys can be fully adopted for the amorphous thermal spray coatings and have both excellent properties and economic advantages.

IV. CONCLUSIONS

In this study, cost-effective Fe-based amorphous alloys used for thermal spray coatings were developed by varying contents of P and C, and their microstructure, hardness, and corrosion resistance were evaluated to reach the following conclusions.

1. Based on representative alloy composition, Fe₇₈Al₂P_(18.3-x)C_xB_{1.7}, P and C contents were varied to calculate driving force of formation of crystalline phases of Fe₃C, α-Fe, γ-Fe, Fe₃P, and Fe₂₃C₆ using the thermodynamic database. The preliminary thermodynamic calculation results showed that only phases of Fe₃P and Fe₃C were formed in the Fe₇₈Al₂P_(18.3-x)C_xB_{1.7} alloy system. Considering the

intersection of driving force curves of Fe₃P and Fe₃C, the carbon contents were selected to be 6.90 and 7.47 at. pct, when the thermodynamic calculation temperatures were 697 K (414 °C) and 715 K (442 °C), respectively.

- According to the microstructure analysis of suction-cast Fe-based alloys, the Fe₇₈Al₂P_{10.83}C_{7.47}B_{1.7} (7.47C) alloy had a fully amorphous microstructure, but Fe₃P and Fe₃C were formed in the Fe₇₈Al₂P_{11.40}C_{6.9}B_{1.7} (6.90C) and Fe₇₈Al₂P_{10.3}C_{8.0}B_{1.7} (8.0C) alloys, respectively. These results were well matched with the thermodynamically calculated data at the crystallization temperature (715 K). Thus, the driving force calculated at 715 K was useful for estimating the amorphous forming ability.
- Cost-effective Fe-based amorphous alloys were successfully designed using the correlation between driving force of phase formation and amorphous forming ability. Particularly, the suction-cast 7.47C alloy could have a completely amorphous microstructure with a maximum thickness of 1.2 mm at least. This alloy also showed a better hardness and corrosion resistance than those of conventional thermal spray coating alloys, and the production cost could be lowered due to the cheaper price of alloying elements, thereby leading to the practical application for amorphous thermal spray coatings.

ACKNOWLEDGMENTS

This work was supported by POSCO under contract No. 2010Y114. The authors would like to thank Dr. Hyung-Jun Kim and Jin Hong Kim of the Research Institute of Industrial Science and Technology (RIST) for their help with fabrication of the Fe-based amorphous alloys.

REFERENCES

- A. Inoue, T. Zhang, and T. Masumoto: *Mater. Trans., JIM*, 1990, vol. 31, pp. 425–28.
- A. Inoue, T. Zhang, N. Nishiyama, K. Ohba, and T. Masumoto: *Mater. Trans., JIM*, 1993, vol. 34, pp. 1234–37.
- W.B. Kim, B.J. Ye, and S. Yi: *Met. Mater. Int.*, 2004, vol. 10, pp. 1–5.
- A. Peker and W.L. Johnson: *Appl. Phys. Lett.*, 1993, vol. 63, pp. 2342–45.
- A. Inoue: *Acta Mater.*, 2000, vol. 48, pp. 279–306.
- X.H. Lin and W.L. Johnson: *J. Appl. Phys.*, 1995, vol. 78, pp. 6514–19.
- D.H. Bae, H.K. Kim, S.H. Kim, D.H. Kim, and W.T. Kim: *Acta Mater.*, 2002, vol. 50, pp. 1749–59.
- H. Shin, Y. Jung, and J. Lee: *Met. Mater. Int.*, 2012, vol. 18, pp. 685–89.
- T. Egami, P.J. Flanders, and C.D. Graham, Jr: *Appl. Phys. Lett.*, 1975, vol. 26, pp. 128–30.
- Z.P. Lu and C.T. Liu: *Acta Mater.*, 2002, vol. 50, pp. 3501–12.
- A. Inoue, W. Zhang, T. Zhang, and K. Kurosaka: *Acta Mater.*, 2001, vol. 29, pp. 2645–52.
- W.L. Johnson: *MRS Bull.*, 1999, vol. 24, pp. 42–56.
- V.D.N. Rao, D.M. Kabat, H.A. Cikanek, C.A. Fucinari, and G. Wuest: *Material Systems for Cylinder Bore Applications Plasma Spray Technology*, SAE, 1997, pp. 107–32.
- G. Barbezat and G. Wuest: *Surf. Eng.*, 1998, vol. 14, pp. 113–16.
- X. Ji, S. Jiang, H. Li, C. Yan, and L. Jiang: *Met. Mater. Int.*, 2012, vol. 18, pp. 655–60.
- D.J. Branagan, W.D. Swank, D.C. Haggard, and J.R. Fincke: *Metall. Mater. Trans. A*, 2001, vol. 32A, pp. 2615–21.
- H. Kim, K. Lim, B. Seong, and C. Park: *J. Mater. Sci.*, 2001, vol. 36, pp. 49–54.
- P. Fauchais, G. Montavon, and G. Bertrand: *J. Therm. Spray Technol.*, 2010, vol. 19, pp. 56–80.
- K. Asami and K. Hashimoto: *Corros. Sci.*, 1984, vol. 24, pp. 83–97.
- K. Kishitake, H. Era, and F. Otsubo: *J. Therm. Spray Technol.*, 1996, vol. 5, pp. 476–82.
- A. Inoue and J.S. Gook: *Mater. Trans., JIM*, 1995, vol. 36, pp. 1180–83.
- H. Li and S. Yi: *Mater. Sci. Eng.*, 2007, vol. A449, pp. 189–92.
- H.W. Sheng, W.K. Luo, F.M. Alamgir, J.M. Bai, and E. Ma: *Nature*, 2006, vol. 439, pp. 419–25.
- Y. Wu, X.D. Hui, Z.P. Lu, Z.Y. Liu, L. Liang, and G.L. Chen: *J. Alloys Compd.*, 2009, vol. 467, pp. 187–90.
- D. Musser, C.L. Chien, and H.S. Chen: *J. Appl. Phys.*, 1979, vol. 50, pp. 7659–61.
- A. Inoue, A. Takeuchi, and T. Zhang: *Metall. Mater. Trans. A*, 1998, vol. 29A, pp. 1779–93.
- M.G. Scott and P. Ramachandrarao: *Mater. Sci. Eng.*, 1977, vol. A29, pp. 137–44.
- D. Kim, B.-J. Lee, and N.J. Kim: *Scripta Mater.*, 2005, vol. 52, pp. 969–72.
- B. Sundman, B. Jansson, and J.-O. Andersson: *CALPHAD*, 1985, vol. 9, pp. 153–90.
- TCFE2000: The Thermo-Calc Steels Database, upgraded by B.-J. Lee and B. Sundman at KTH, Stockholm, 1999.
- B.-J. Lee: Pohang University of Science and Technology (POSTECH), Korea, unpublished update of thermodynamic database.
- J.-H. Shim, C.-S. Oh, and D.N. Lee: *J. Korean Inst. Met. Mater.*, 1996, vol. 34, pp. 1385–93.
- V. Raghavan: *Phase Diagrams of Ternary Iron Alloys*, Indian Institute of Metals, Calcutta, 1988.
- M. Komaki, T. Mimura, R. Kurahasi, M. Kouzaki, and T. Yamasaki: *Mater. Trans. JIM.*, 2011, vol. 52, pp. 474–80.
- T.E. Lister, R.N. Wright, P.J. Pinhero, and W.D. Swank: *J. Therm. Spray Technol.*, 2002, vol. 11, pp. 530–35.
- Y. Huang, Y. Guo, H. Fan, and J. Shen: *Mater. Lett.*, 2012, vol. 89, pp. 229–32.
- Z. Zhou, L. Wang, F. Wang, and Y. Liu: *Trans. Nonferrous Met. Soc. China*, 2009, vol. 19, pp. 634–38.
- V.R. Raju, F. Schneider, W. Schwarz, J. Eckert, and A. Gebert: *Mater. Corr.*, 2002, vol. 53, pp. 85–90.
- S.L. Wang, H.X. Li, S.Y. Hwang, S.D. Choi, and S. Yi: *Met. Mater. Int.*, 2012, vol. 18, pp. 607–12.
- S.L. Wang, H.X. Li, Y.U. Jeong, and S. Yi: *Met. Mater. Int.*, 2012, vol. 18, pp. 791–97.
- London Metal Exchange (January 13th of 2012). <http://www.lme.com>.